Chemical Physics 558 (2022) 111518

Contents lists available at ScienceDirect

Chemical Physics

journal homepage: www.elsevier.com/locate/chemphys

Absence of isotope effects in the photo-induced desorption of CO from saturated Pd(111) at high laser fluence

A.S. Muzas [b,*], Alfredo Serrano Jiménez [b], Juraj Ovčar [d], Ivor Lončarić [d,a], Maite Alducin [b,a], J. Iñaki Juaristi [c,a,*]

[a] Donostia International Physics Center (DIPC), Paseo Manuel de Lardizabal 4, 20018 Donostia-San Sebastián, Spain
[b] Centro de Física de Materiales CFM/MPC (CSIC-UPV/EHU), Paseo Manuel de Lardizabal 5, 20018 Donostia-San Sebastián, Spain
[c] Departamento de Polímeros y Materiales Avanzados: Física, Química y Tecnología, Facultad de Químicas UPV/EHU, Apartado 1072, 20080 Donostia-San Sebastián, Spain
[d] Ruđer Bošković Institute, Bijenička 54, HR-10000 Zagreb, Croatia

ARTICLE INFO

Keywords:
Photo-induced desorption
Isotope effect
Carbon monoxide
Palladium surface
Neural network
Langevin dynamics

ABSTRACT

Neural network-based potential energy surfaces are currently gaining relevance in the context of gas-solid dynamics. In this work, we use this methodology to theoretically explore femtosecond laser pulse induced desorption of CO from the Pd(111) surface with a coverage of 0.75 ML. We performed molecular dynamics simulations in the high laser fluence regime on two different CO isotopes, $^{12}C^{16}O$ and $^{13}C^{18}O$, in order to search for possible isotope effects affecting the photo-induced desorption. According to our findings, isotope effects of relevance do not appear in desorption probabilities once the whole process has finished after 50 ps. However, for those molecules desorbed with the highest translational kinetic energies, we obtain that $^{12}C^{16}O$ molecules are more vibrationally excited than $^{13}C^{18}O$. This mostly happens as a consequence of the interaction of adsorbed CO with the laser-excited electrons in the substrate.

1. Introduction

An effective procedure to induce chemical reactions, diffusion, and desorption in metal surfaces decorated with adsorbates consists of irradiating the system with high-fluence (~10 J/m^2) femtosecond laser pulses [1–3]. At the usual ultraviolet, visible, and near-infrared wavelengths, the laser light is absorbed in a substantial proportion by the metal by exciting electrons that rapidly thermalize. During their deexcitation, electrons couple with surface phonons. Interplay of (direct) electronic- and (indirect) phononic-driven energy transfer to adsorbates can trigger the aforementioned photo-induced phenomenology, including processes that cannot be thermally activated [4–9]. The time scale of adsorbate–substrate interactions and hence the dominance of electrons or phonons in the photo-induced dynamics can be determined experimentally with two pulse correlation (2PC) measurements [1,4–11]. In addition, the search of isotope effects has been used as a complementary tool to disentangle whether electronic or phononic excitations govern the femtosecond laser pulse induced desorption, being its presence a fingerprint of electron-mediated interactions [1,6,11–13]. In this respect, experimental measurements have been performed in different adsorbate–surface systems. For instance, remarkable isotope effects have been found in the oxidative desorption for the O + CO/Ru (0001) system [6,12], the recombinative desorption of H_2 and D_2 from H (D)-saturated Ru(0001) [7], and the recombinative desorption of O_2 from the O-covered Pd(111) surface [13]. However, systems in which the isotope effect is absent such as CO desorption from Ru(0001) have also been reported [11].

From the theoretical side, a reliable description of the complex photo-induced desorption dynamics consists in combining the two temperature model [14], which describes the electronic and phononic excitations in terms of two coupled thermal baths, with molecular dynamics with electronic friction (MDEF) description of the adsorbates dynamics [3,15,16]. Simulations based on this methodology have been successfully applied to understand different photo-induced desorption experiments [17–24], including the strong isotope effect observed in the recombinative desorption of H_2 and D_2 from the H(D)-saturated Ru (0001) surface [18]. An important ingredient in these simulations was the use of six-dimensional potential energy surfaces (PESs) that, being based on density functional theory (DFT) calculations, accurately account for the dominant adsorbate–surface interaction.

* Corresponding authors.
E-mail addresses: albertopablo.sanchez@ehu.eus (A.S. Muzas), josebainaki.juaristi@ehu.eus (J.I. Juaristi).

https://doi.org/10.1016/j.chemphys.2022.111518
Received 26 October 2021; Received in revised form 18 February 2022; Accepted 20 March 2022
Available online 23 March 2022
0301-0104/© 2022 The Authors. Published by Elsevier B.V. This is an open access article under the CC BY-NC-ND license (http://creativecommons.org/licenses/by-nc-nd/4.0/).

Including surface atoms movements, additional adsorbates, and polyatomic molecules became a difficult task due to the increasing complexity of the interpolation methods that were used to construct accurate PESs. In this respect, the posterior ab initio molecular dynamics with electronic friction (AIMDEF) model represented a step forward to treat within DFT the full-multidimensional nonadiabatic dynamics of atoms and molecules on metal surfaces [25]. It has been used to describe, among other processes, adsorption and further relaxation of hot atoms and molecules on diverse metal surfaces [26–32], adsorption and scattering of molecules [33,34], Eley–Rideal and hot atom abstraction processes [35–37], the vibrational lifetime of adsorbed H_2 on Pb films [38], and also the existence of isotope effects in the H_2/D_2 photo-desorption from the Ru(0001) surface [39]. Its extension including time-dependent electronic (T_e) [39] and phononic (T_l) temperatures [(T_e,T_l)-AIMDEF] [40] has allowed describing femtosecond laser-induced dynamics for systems with multiple degrees of freedom, including the individual movement of surface atoms and, importantly, of multiple adsorbates at finite coverages. However, the high computational cost of evaluating DFT atomic forces at every single integration step severely limits both the statistics and integration time of the process under study.

A straightforward reduction of these limitations is achieved by using a molecular dynamics approach, in which an explicit PES or force field is employed as a force generator. In this regard, multidimensional PESs based on machine learning techniques offer a computationally fast alternative to classic force fields while still maintaining the ability to reproduce ab initio results [41], provided that the correct training is performed [42]. In particular, neural network (NN) based molecular dynamics approaches have become relevant in recent years with a growing number of examples in different areas, such as solid–liquid water surfaces [43–45] and gas–solid interfaces [46–58]. After the breakthrough of the atomistic neural network model [59], and with incorporation of its postulates, different NN approaches for molecular dynamics have been developed [60]. Amongst them, the embedded atom neural network (EANN) framework [32,61,62] offers interesting possibilities to train accurate NN-PESs able to describe systems containing several independently moving atoms and thus many degrees of freedom. In addition, it allows to span wide ranges of temperature and multiple changes in adsorbate coverages, which are typical features of gas–solid photodesorption dynamics.

This molecular dynamics approach, hereinafter called (T_e,T_l)-MDEF, opens the possibility of new and more complete theoretical studies that were not feasible in reasonable time with the (T_e,T_l)-AIMDEF methodology. For example, despite AIMDEF being able to describe isotope effects in the femtosecond laser induced recombinative desorption of H_2 and D_2 from H(D)-Ru(0001) [39], it was difficult to perform the same type of calculations for a system with heavier adsorbates, like CO adsorbed on Pd(111). In the first case, the coupling of adsorbates with lattice degrees of freedom (DOFs) could be disregarded due to the adsorbate–substrate mass mismatch, reducing the dimensionality of the problem. However, a good description of CO/Pd(111) cannot neglect this mechanism of desorption, which could in addition increase the amount of dynamics time to describe the complete process by several tens of picoseconds, as it will be indeed demonstrated in Section 3. For instance, Hong et al. [9] studied the femtosecond laser induced desorption of CO on Pd(111) with 2PC experiments and a three temperature model approach. Their results suggest that the underlying mechanism is dominated by hot electrons-adsorbate interaction, as 2PC spectra could be reproduced by their model with only this photo-desorption channel activated. However, some 2PC spectra exhibited time delays typically associated with a phonon driven process. Since an accurate EANN-PES for simulating the photo-induced desorption of CO from the Pd(111) surface with an initial coverage of 0.75 ML is now available [63], this kind of study becomes feasible with an atomistic model. Therefore, in this work the photo-induced CO desorption process on Pd(111) has been simulated for two different CO isotopes, the light $^{12}C^{16}O$ and the heavy $^{13}C^{18}O$, and thus analyzed from a theoretical perspective in order to contribute to the study of the underlying mechanism of desorption.

The present paper is structured in the following way. The main theoretical features for the system under study, the utilized photo-desorption model, as well as the physical quantities of relevance analyzed in the simulations are explained in Section 2. The MDEF results for both studied isotopes are discussed in Section 3. Finally, our findings are summarized in Section 4.

2. Theoretical methods

We simulated the femtosecond laser-induced desorption of CO from a Pd(111) surface with an initial CO coverage of 0.75 ML following the classical molecular dynamics model proposed in Ref. [63]. In this model, the desorption process is simulated using two separated dynamical systems. On the one hand, the macroscopic interaction of Pd with the femtosecond laser pulse is described by two thermal baths, one representing the excited electrons, characterised by temperature $T_e(t)$, and one representing the excited lattice, characterised by temperature $T_l(t)$. The flow of energy from the laser pulse to the thermal baths is modelled with a set of coupled heat equations. This is a standard approach known as the two-temperature model (2TM) [14] that accounts for laser to electrons energy flow, electrons to lattice energy flow, and electrons energy dissipation by diffusion. The dynamics of this macroscopic energy exchange is governed by the electron and lattice heat capacities, the electron–phonon coupling constant, and the electron thermal conductivity of palladium. Details of the choice of these properties are published elsewhere [64]. On the other hand, the microscopical response of the adsorbate–surface system is simulated with a periodic atomistic model containing six CO adsorbates placed pairwise on the top, hcp, and fcc sites of a (4×2) Pd(111) four-layer surface, as shown in Fig. 1. The dynamics of this atomistic model is described by a set of coupled

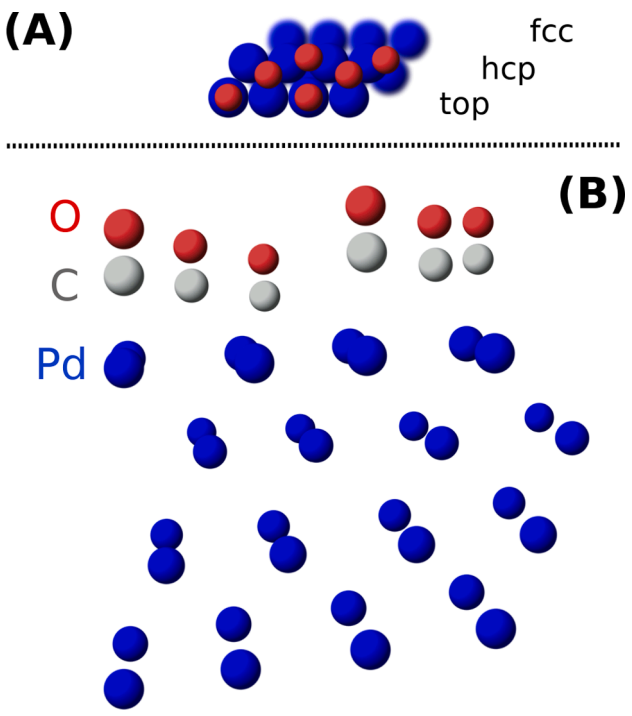

Fig. 1. Schematic representation of the 0.75ML CO/Pd(111) cell, showing O atoms in red, C in grey, and Pd in blue. (A) Top orthogonal view, showing CO top, hcp, and fcc adsorption sites on topmost (blue) and second topmost (blurred blue) surface layers. (B) Perspective view. (For interpretation of the references to colour in this figure legend, the reader is referred to the web version of this article.)

equations of motion (EOMs). Langevin-like EOMs with electronic friction [25–30,38–40] are used for CO motion to describe the coupling of the molecules to the electronic system with temperature $T_e(t)$. The Pd atoms of the first two surface layers are coupled to a Nosé-Hoover thermostat [65,66] with temperature $T_l(t)$. The third Pd layer is described by regular adiabatic EOMs, whilst the fourth layer is left frozen. It is worth to stress out that both $T_e(t)$ and $T_l(t)$ are calculated with the 2TM heat equations independently of the time evolution of the atomistic model. Therefore, the micro description of the system (atomistic model) is forced to follow the macro description of the Pd-laser interaction (2TM) by utilising the time dependent temperature of the thermal baths as the driving temperature of the thermostats used in the EOMs.

Here, all adiabatic force terms were computed with the best performing EANN [61] PES presented in Ref. [63]. The electronic friction coefficients used in Langevin EOMs were calculated under the local density friction approximation (LDFA) [67] that requires the knowledge of the surface electron density at the position of each atom forming the CO adsorbate. As detailed in Ref. [63], the latter is calculated at each integration step with a computationally efficient and accurate density generator function. This function was obtained by fitting the surface electron density data extracted from the (T_e,T_l)-AIMDEF simulations [40] to a sum of exponential functions, each centered at the position of the Pd surface atoms.

In order to study whether isotope effects arise in the femtosecond laser induced desorption of CO in the 0.75ML-CO/Pd(111) system, we considered two different CO isotopes, namely $^{12}C^{16}O$ and $^{13}C^{18}O$. For each of them, we performed 2000 (T_e,T_l)-MDEF calculations using an integration time-step of 0.2 fs. The initial conditions were obtained by fully thermalizing the starting configurations used in previous (T_e,T_l)-AIMDEF calculations [40] to 90 K. In addition to (T_e,T_l)-MDEF dynamics, and in order to disentangle the role that the different kinds of thermal excitations (electron- or phonon-mediated) have in the desorption for each CO isotope, we generated an extra set of 2000 trajectories, named T_l-MDEF. This batch includes only the effect of the excited phonons by setting the electron friction coefficients equal to zero in the adsorbates Langevin EOMs. All calculations were performed for a incident $sech^2$ laser pulse of wavelength 780 nm, absorbed fluence 130 J/m^2, and time full width at half maximum of 100 fs.

Taking advantage of the MDEF approach used in this work, all our dynamics calculations were extended up to 50 ps (see Section 3), 12 times longer than prior AIMDEF-based studies [40]. This could potentially introduce PES extrapolation errors, since the calculated trajectories may have explored configurations out of the confidence zone of the trained EANN-PES, as it was prepared with configurations extracted from 4 ps AIMDEF. For the purpose of addressing the quality of our 50 ps trajectories, we have controlled all our visited configurations each 100 fs by means of a distance function that measures how "far" they are from the training set used to generate the EANN-PES. The idea is that the closer these configurations are to the training set, the more reliable their description by the EANN-PES is, minimizing possible extrapolation errors. This general concept has been widely used in problems related to PES systematic improvement methods [68–70], and novelty sampling algorithms [71,72]. For a better comprehension of how we define the distance function, we proceed to quickly review the relevant components of a EANN-PES.

The final expression of a EANN-PES can be defined as:

$$V\left(\mathscr{R}\right) = \sum_{i\in\mathscr{R}} NN_{\tau_i}[\boldsymbol{\rho}(i)], \tag{1}$$

where $\mathscr{R}$ is the set of all atoms $i = (\mathbf{R}_i, \tau_i)$ of a specific system configuration, each of them characterized by its Cartesian coordinates $\mathbf{R}_i$ and its atomic type τ_i (in our case C, O, and Pd), and $NN_{\tau_i}[\boldsymbol{\rho}(i)]$ is the neural network trained to give the energy contribution of atom i of type τ_i based on its environment, described by density vector $\boldsymbol{\rho}(i)$ with components $\rho_{L,\alpha,r_s}(i)$ given by:

$$\rho_{L,\alpha,r_s}\left(i\right) = \sum_{l_x,l_y,l_z}^{l_x+l_y+l_z=L} \frac{L!}{l_x!l_y!l_z!}\left(\sum_{j\in\mathscr{R}\setminus\{i\}} c_j \phi^{\alpha,r_s}_{l_x,l_y,l_z}\left(\left|\mathbf{R}_i - \mathbf{R}_j\right|\right)\right)^2, \tag{2}$$

with $L \in \{0,1,2,\ldots,L_{\max}\}$ and $(\alpha, r_s) \in \{(\alpha_0, r_{s0}), (\alpha_1, r_{s1}), \ldots(\alpha_\eta, r_{s\eta})\}$ being the specific values (α_i, r_{si}) chosen using the method presented in Supplementary Information of Ref. [54]. Functions $\phi^{\alpha,r_s}_{l_x,l_y,l_z}(|\mathbf{R}_i - \mathbf{R}_j|)$ stand for Gaussian type orbitals (GTOs) as described in Ref. [54]. Indexes l_x, l_y, and l_z stand for the orbital momentum components of the GTOs, index α their width, and index r_s their center. The choice of indexes L,α, and r_s define the dimension of the environment density vector $\boldsymbol{\rho}$, and is kept constant for all neural networks NN_{τ_i}. In our case, $L_{\max} = 3$ and $\eta = 14$, thus each atom environment is described by a 60-dimensional density array. With all this in mind, we define the distance between two environments centered at atoms $i \in \mathscr{R}$ and $j \in \mathscr{R}'$ of type τ that may come from different system configurations $\mathscr{R}$ and $\mathscr{R}'$ as:

$$\mu_\tau\left(i,j\right) = |\boldsymbol{\rho}(i) - \boldsymbol{\rho}(j)| = \sqrt{\sum_{(L,\alpha,r_s)} \left(\rho_{L,\alpha,r_s}(i) - \rho_{L,\alpha,r_s}(j)\right)^2}, \tag{3}$$

i.e., the Euclidean norm of the difference of their density descriptors. The advantage of this measure compared with a regular $|\mathbf{R}_i - \mathbf{R}_j|$ distance is that $\boldsymbol{\rho}$ arrays are already symmetrized, and that they are the natural input layer of each of the neural networks used to define the potential. However, the specific values of μ_τ are only consistent given a specific training state, as functions ρ_{L,α,r_s} depend on coefficients (labeled as c_j in Eq. 2) that are fitted during the training procedure. Also, $\mu_\tau(i,j) = 0$ ensures that the individual energy contribution of atoms i and j to their respective configurations, $NN_\tau[\boldsymbol{\rho}(i)]$ and $NN_\tau[\boldsymbol{\rho}(j)]$ is the same. A similar metric has been used elsewhere [70] with success as a mean of measure geometric similarities between configurations to include in EANN-PES for systematic trajectory-free improvement. Now, if we have a collection of system configurations $\Re = \{\mathscr{R}\}$, we can define the distance between this set and a given environment i of type τ as:

$$d^\tau_{min}(i,\Re) = \min\left\{\mu_\tau(i,j) : j \in \mathscr{R}, \tau_j = \tau, \mathscr{R} \in \Re\right\}, \tag{4}$$

i.e., $d^\tau_{\min}(i,\Re)$ is the smallest μ_τ distance between all environments centered at atoms of type τ from every configuration inside $\Re$. Therefore, when $d^\tau_{\min}(i) \to 0$ there is an environment within all configurations in $\Re$ that is similar to i. Hereinafter, we drop the $\Re$ dependence of $d^\tau_{\min}$ and assume that $\Re$ is just the training set of our EANN-PES.

Top panels of Fig. 2 show the absolute error in EANN-PES atomic forces $|\mathbf{F}^{\text{EANN}}_i - \mathbf{F}^{\text{DFT}}_i|$ centered at each atom i coming from the entire set of 4 ps AIMDEF configurations (except training configurations) from Ref. [40] as a function of $d^\tau_{\min}(i)$ for atomic types τ equal to C (gray points, top left panel), O (red points, top middle panel) and Pd (bluish points, top right panel). In the latter case, we have distinguished Pd atoms belonging to the first (dark blue), second (blue), and third layer (light blue). Black lines and black shadowed areas represent the average and standard deviation of absolute force errors for AIMDEF environments at a given $d^\tau_{\min}$ distance from the training set. In order to guide the eye, we have also included in orange the average (dashed line), and standard deviation (shadowed area) of absolute force errors in the training set. From these panels, we can see a clear correlation between the increase of the minimum distance to the training set and the increase of the average absolute error and error dispersion in the atomic forces predicted by the EANN-PES. This is independent of the specific atomic type in question, corroborating the initial intuitive hypothesis that atomic environments that are closer (according to our definition) to atomic environments included in the training set tend to be better described by the PES. This also indicates that the specific choice of the metric μ_τ as an Euclidean norm is enough to distinguish efficiently

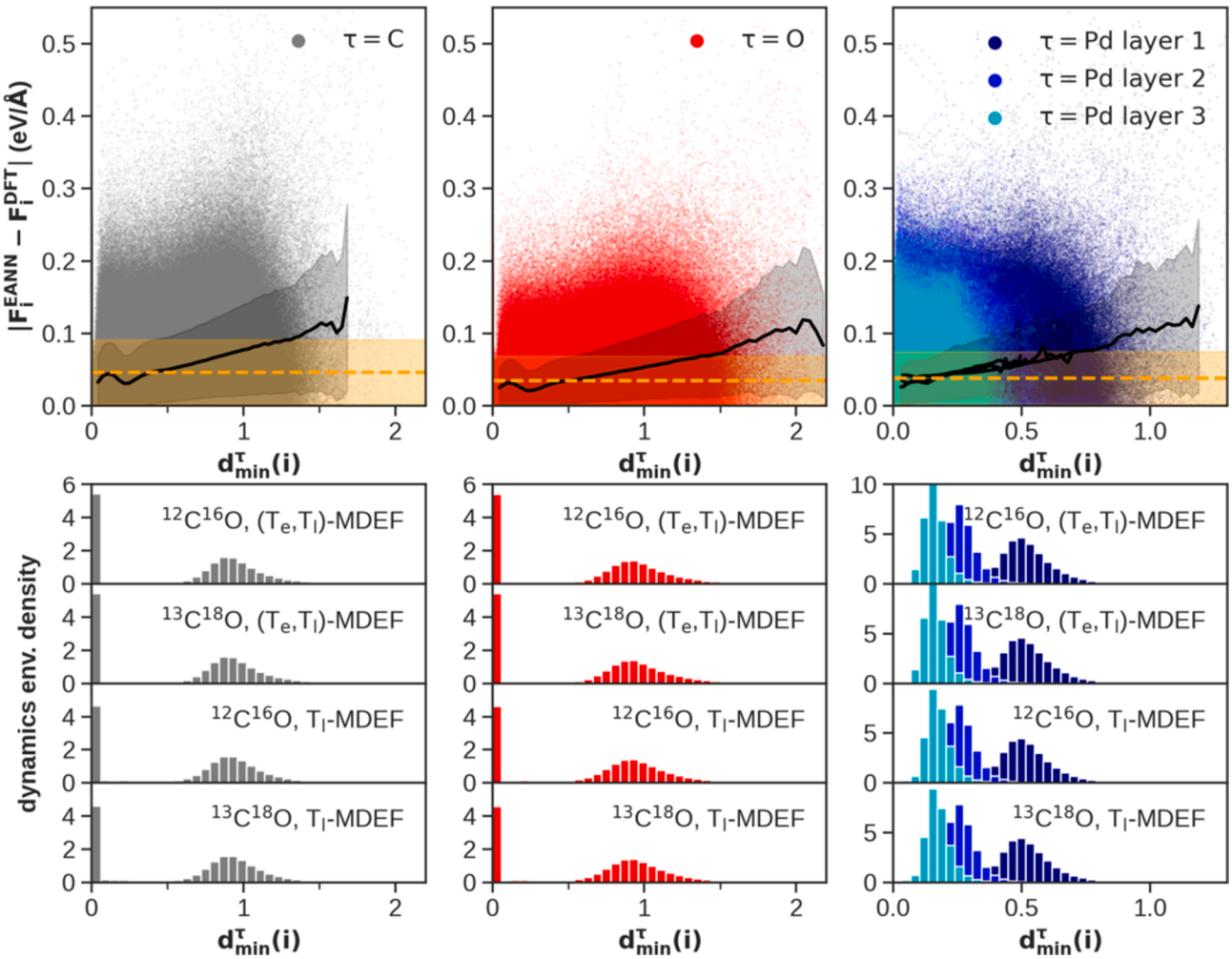

Fig. 2. Top panels: EANN-PES absolute error in atomic forces for original AIMDEF configurations [40] as a function of minimum environmental distance to the training set (colored dots). Black lines and black shadowed areas represent the average and standard deviation of absolute force errors of the data shown for each d^{τ}_{min} value, whereas orange lines and orange shadowed areas stand for the average and standard deviation of absolute force errors in the training set. Bottom panels: normalized density distribution of a representative subset of environments visited during all our 50 ps MDEF simulations (see text) as a function of their distance to the EANN-PES training set. Results for C atoms are shown in gray (left panels) and for O in red (middle panels). In the case of Pd atoms, results for the first layer are shown in dark blue, for the second in blue, and for the third in light blue (right panels). (For interpretation of the references to colour in this figure legend, the reader is referred to the web version of this article.)

between visited environments in the 60 dimensional space of $\boldsymbol{\rho}$. Given that the EANN-PES used in this work was demonstrated to reproduce AIMDEF results accurately elsewhere [63], we proceed to use the distribution of environment distances analyzed in these panels to benchmark the distribution of minimum environment distances encountered during our dynamics, as we can now associate a representative mean absolute error in atomic forces for each value of d^{τ}_{min}.

Fig. 2 (bottom panels) shows the normalized density distribution of environments visited during our 50 ps MDEF simulations as a function of their distance to the EANN-PES training set, following the same color code as in top panels. Each bottom subpanel is devoted to the results of (T_e,T_l)-MDEF and T_l-MDEF applied to the heavy CO isotopes ($^{13}C^{18}O$) and light CO isotopes ($^{12}C^{16}O$). The C and O distributions exhibit a sharp density peak close to $d^{C,O}_{min} = 0$, coming mainly from environments of desorbed CO molecules, and a Gaussian-like distribution centered around $d^{C,O}_{min} = 0.9$, coming from environments of adsorbed CO molecules. In the case of Pd panels, it is observed how depending on the layer, environment distributions are Gaussian-like distributions centered at d^{Pd}_{min} equal to 0.2, 0.3, and 0.5 for 3rd, 2nd, and 1st Pd layer, respectively. From the comparison between the different types of MDEF, isotope weights, and atom types, the distribution of environments as a function of d^{τ}_{min} remains unchanged, which means that there are no big differences in terms of distance to the training set between the atomic environments formed during these simulations. They are equally "similar" to the training set. If we compare now these distributions with those of AIMDEF calculations (top panels), we find that most of our dynamics environment density distributions remain within distances explored during AIMDEF calculations, i.e., we do not find a significant amount of atomic environments farther from the training set than those explored during AIMDEF calculations. It is also apparent that all MDEF environment distributions maxima lay in an intermediate region of d^{τ}_{min} values, where the associated mean absolute error in forces of AIMDEF calculations, whilst still small, is higher than the average in the training set. These findings support that our long dynamics calculations are not fundamentally different from previous AIMDEF calculations and that the used EANN-PES is still applicable with no further retraining.

Now that we have addressed the reliability of our 50 ps dynamics, let us focus on the relevant quantities used in Section 3 to describe the physics of (T_e,T_l)-MDEF and T_l-MDEF calculations. To begin with, we consider the time dependent CO desorption probability $P(t)$ as the average of the number of desorbed CO molecules at a given time t in the ensemble, $N_{CO}(t)$, divided by the total number of CO molecules in the

ensemble, $6N_{traj}$, where N_{traj} is the number of performed trajectories (in our case 2000), i.e., $P(t) = N_{CO}(t)/(6N_{traj})$. Based on this definition of the CO desorption probability and the usual text-book definition of desorption rate as the minus rate of change of the surface coverage, it is easy to derive a mean time dependent desorption rate $R(t)$ defined as $R(t) = \theta_0 dP(t)/dt$, being θ_0 the initial CO coverage of the surface, which in our case is 0.75 ML. Another relevant quantity in our analysis is the vibrational state of desorbed CO molecules, v. Following the quasi-classical action-angle variable approach of Ref. [73], v is defined as the closest integer value fulfilling the condition $v = \frac{\alpha}{\hbar} - \frac{1}{2}$, with h being the Planck constant and α the vibrational action defined as:

$$\alpha = \oint dr\, p_r = \frac{1}{\pi}\int_{r_{in}}^{r_{out}} dr \sqrt{2\mu\left(E_{CO} - V\left(r\right) - \frac{L^2}{2\mu r^2}\right)}\,, \tag{5}$$

where p_r is the desorbed CO vibrational momentum, μ is its reduced mass, r_{out} and r_{in} are the outer and inner turning points of the CO vibrational motion, E_{CO} is its total internal energy, $V(r)$ is the CO vibrational potential in vacuum (here given by the EANN PES) and L is the total angular momentum.

3. Results and discussion

As a starting point, let us focus on the time evolution of the CO desorption probability during the first 4 ps, in consonance with what was considered in prior (T_e,T_l)-AIMDEF calculations [40]. Fig. 3 shows that there are little differences in the desorption probability for both isotopes when considering either (T_e,T_l)-MDEF (full lines) or T_l-MDEF (dashed lines) results, being blue and red lines the time evolution of the light ($^{12}C^{16}O$) and heavy ($^{13}C^{18}O$) isotope desorption, respectively. Shaded regions around each curve are statistical uncertainty intervals calculated in the framework of Wilson score intervals [74] assuming a 99% of confidence. On a closer look, although these differences are small, the desorption probability of $^{12}C^{16}O$ at a given time is always higher than for $^{13}C^{18}O$ in the whole 4 ps interval. This is consistent with an overall higher acceleration that the lighter CO molecules may experience due to the mass dependency of the EOMs, which helps them to overcome faster the desorption barrier. Interestingly, the differences between $^{12}C^{16}O$ and $^{13}C^{18}O$ are reduced when the interaction with the electron bath is switched off in T_l-MDEF calculations, which is in consonance with the expected lack of isotope effects when phonon-mediated desorption mechanism dominates. This yield us the conclusion that at least for the first 4 ps, the higher differences between the light and the heavy CO isotopes shown in (T_e,T_l)-MDEF results, despite small, come indeed from the interaction with the laser-excited electrons rather than from an adiabatic coupling to surface DOFs.

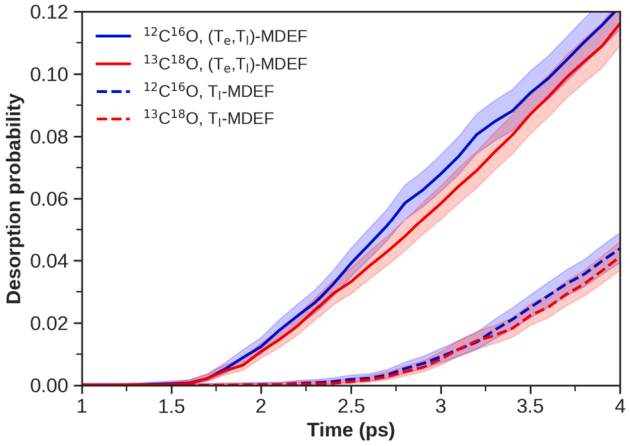

Fig. 3. Time evolution of the desorption probability obtained during the initial 4 ps. Results for $^{12}C^{16}O$ (blue lines) and $^{13}C^{18}O$ (red lines). Full and dashed lines stand for (T_e,T_l)-MDEF and T_l-MDEF calculations, respectively. Shaded areas are statistical uncertainty intervals calculated within the framework of Wilson score intervals [74] assuming a 99% of confidence.

It is clear from Fig. 3 that both (T_e,T_l)-MDEF and T_l-MDEF CO desorption probabilities keep increasing with time beyond the 4 ps (T_e, T_l)-AIMDEF milestone. In this respect, a relevant question is whether the subtle isotope effect observed on (T_e,T_l)-MDEF for $t \lesssim 4$ ps changes when CO desorption reaches its saturation point, i.e., when the whole desorption process has finished completely. Taking advantage of the EANN-PES low computational evaluation cost, we extended the dynamics of both ensembles up to 50 ps. As seen in Fig. 4 (top panel), the desorption probabilities of both isotopes (same color code as in Fig. 3) saturate to the same value of ≈ 0.35 in the case of (T_e,T_l)-MDEF (full lines), and of ≈ 0.34 in the case of T_l-MDEF (dashed lines). Thus, the isotope differences found in (T_e,T_l)-MDEF calculations during the initial 4 ps not only do not increase at longer times, but they are negligible with the increase of desorption probability. This behavior is consistent with the phonon-mediated desorption mechanism dominating over the electron-mediated one after the initial stages of the dynamics. This is supported by the convergence of both CO desorption probabilities to almost the same saturation value, being the T_l-MDEF saturated desorption probability only 1% lower than for (T_e,T_l)-MDEF. This can be explained by the fact that the lattice mean temperature between 4 and 50 ps varies from ≈ 1200 K to 700 K for the chosen high laser fluence. Therefore, even if during the first stages of the dynamics the electronic-mediated desorption mechanism is important, as reflected in the high difference in desorption probability found between (T_e,T_l)-MDEF and T_l-MDEF in Fig. 3 and the subtle isotope effect, at later times the lattice temperature is high enough to dominate the desorption process regardless of whether the interaction with the electronic bath is present or not.

A different perspective on the CO desorption dynamics is achieved when studying the time evolution of the desorption rate $R(t)$, as

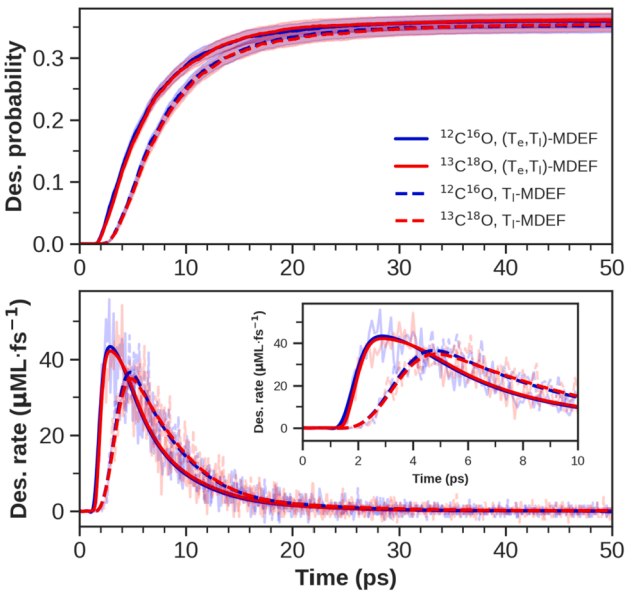

Fig. 4. Time evolution of the desorption probability (top) and corresponding desorption rate (bottom) obtained during 50 ps. Bottom inset shows desorption rates during the first 10 ps. Blue lines stand for $^{12}C^{16}O$ results. Red lines stand for $^{13}C^{18}O$ results. Full and dashed lines correspond to (T_e,T_l)-MDEF and T_l-MDEF calculations, respectively. Raw noisy desorption rates (bottom panel, blurry lines) were obtained from desorption probabilities by numerical differentiation. Smooth desorption rates (bottom panel, thick lines) were obtained after applying a fifth order noise-reduction spline interpolation over raw desorption probabilities. (For interpretation of the references to colour in this figure legend, the reader is referred to the web version of this article.)

described in Section 2. This is shown in Fig. 4, bottom panel, where the raw results (blurry lines) have been smoothed out by a noise-reducing interpolation with fifth order splines to get the solid and dashed smooth curves. The full 50 ps time interval considered allows us to observe the characteristic functional form of $R(t)$, exhibiting its maxima at 3 ps and 5 ps for (T_e,T_l)-MDEF (full lines) and T_l-MDEF (dashed lines), respectively. As expected from the previous analysis of CO desorption probabilities, one can check the nearly equal desorption rates for both isotopes, $^{12}C^{16}O$ (blue lines) and $^{13}C^{18}O$ (red lines) in both dynamical situations. In addition, it is easy to see now that (T_e,T_l)-MDEF desorption rate reaches higher values in a shorter amount of time, exhibiting a narrower profile than in the case of T_l-MDEF rate. This reinforces our conclusion that despite the absence of any relevant isotope effect in the desorption of CO molecules, interaction with substrate electrons is still important for the description of the desorption dynamics during the first 15 ps.

To further explore the relevance of the coupling of CO DOFs to the excited electrons, now we check if there is any fingerprint of the electron-driven desorption mechanism in the vibrational excitation of desorbed molecules. Fig. 5 shows the proportion of desorbed CO molecules (regarded as a probability) that either stayed in their fundamental vibrational state ($v = 0$) or were vibrationally excited ($v > 0$), with quasiclassical quantum numbers v computed as described in Section 2.

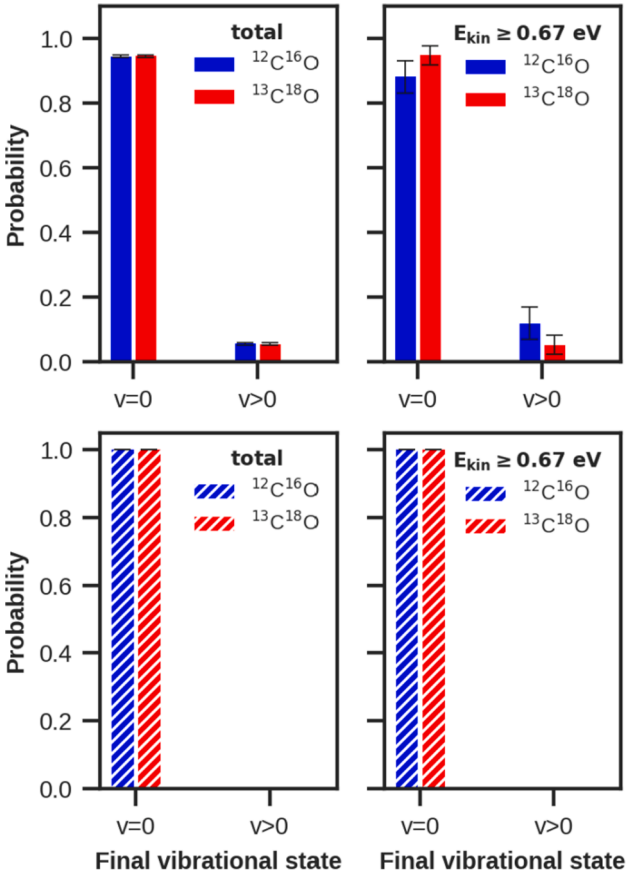

Fig. 5. Quasiclassical evaluation of the proportion of desorbed CO molecules that stayed in their fundamental vibrational state ($v = 0$) or experienced vibrational excitation ($v > 0$). Left panels measure the proportion respect to the total amount of desorbed CO molecules. Right panels measure the proportion only respect to high energetic ($E_{kin} > 0.67$eV) CO molecules (see text). Blue bars stand for $^{12}C^{16}O$ results. Red bars stand for $^{13}C^{18}O$ results. Top (full bars) and bottom (striped bars) panels stand for (T_e,T_l)-MDEF and T_l-MDEF calculations respectively. Error bars represent standard deviation according to binomial distribution. (For interpretation of the references to colour in this figure legend, the reader is referred to the web version of this article.)

Red bars stand for the proportions related to $^{13}C^{18}O$, while blue bars stand for $^{12}C^{16}O$. Full bars (upper panels) refer to results extracted from the (T_e,T_l)-MDEF ensemble, while striped bars (bottom panels) refer to T_l-MDEF. Error bars correspond to the standard deviation of v according to the statistics of a binomial distribution. Analysis of the full desorbing CO ensembles (left column panels of Fig. 5) shows that only when the coupling to the excited electrons is included [(T_e,T_l)-MDEF], there is a small percentage ($\approx 5\%$) of CO molecules that desorb in a vibrationally excited state. This yields us the conclusion that the vibrational energy gain in (T_e,T_l)-MDEF comes mainly from the coupling to the excited electronic system. In addition, it is clear that the amount of vibrational excitation is independent of the mass of the CO isotope under question.

A somewhat different picture appears if we center our attention on CO molecules that desorb with the highest translational kinetic energies, i.e., E_{kin} above 0.67 eV (right panels of Fig. 5). Focusing first on the T_l-MDEF data (bottom right panel), we observe that phonons do not induce any appreciable vibrational excitation even in those CO desorbing with $E_{kin} > 0.67$eV, therefore showing no isotope effect. Since, as stated above, the vibrationally excited CO molecules are mainly caused by the laser-excited electrons, it is more interesting to analyze the (T_e,T_l)-MDEF results (top right panel). In this case, there is a sizeable isotope effect in the vibrational excitation of desorbed CO with $E_{kin} > 0.67$eV in favour of the light isotope: the $^{12}C^{16}O$ vibrational excitation probability is 6% higher than for $^{13}C^{18}O$.

4. Summary and conclusions

We have investigated the femtosecond laser pulse-mediated desorption of two CO isotopes, namely $^{12}C^{16}O$ (light CO) and $^{13}C^{18}O$ (heavy CO), from a Pd(111) surface at 0.75 ML coverage in the high laser fluence regime. A recently developed embedded atom neural network potential energy surface (EANN-PES) for this system [63] which is able to reproduce previous two temperature ab initio molecular dynamics with electronic friction results [40] has been utilized to computationally simulate the photodesorption process for both isotopes. For a maximum time of 50 ps in all cases, sets of 2000 dynamics have been performed for each kind of CO molecule under two different situations. On the one hand, adsorbates were allowed to interact with both electrons and phonons excited by the incoming laser pulse [(T_e,T_l)-MDEF], whereas on the other hand, only interaction with the excited phonons was permitted [T_l-MDEF]. For our model, CO/Pd(111) interface was thermalized to 90 K prior to the femtosecond laser pulse activation. All dynamics calculations were validated with a measure of the environment distance of visited configurations to the training set of the EANN-PES. CO desorption probabilities, desorption rates, and further quasiclassical vibrational excitation analysis have been computed in order to determine whether isotope effects exist for the system or not.

According to the here presented results, isotope effects are absent in the desorption probability of CO from the 0.75 ML precovered Pd(111) surface. The subtle desorption probability difference between $^{12}C^{16}O$ and $^{13}C^{18}O$ found for (T_e,T_l)-MDEF calculations at early dynamical times (below 4 ps) can be completely neglected for longer times (50 ps), when phonon-mediated contribution to desorption dominates over its electronic counterpart and the desorption process has finished completely. This is supported by the fact that (T_e,T_l)-MDEF and T_l-MDEF desorption probability saturation values are almost equal and constant after 50 ps. The latter does not mean that the interaction with the electronic bath can be neglected in the whole desorption process, as CO desorption rates for (T_e,T_l)-MDEF present a sharper and narrower peak compared to T_l-MDEF results. An analysis of the vibrational state of the desorbed molecules shows that vibrational excitation is minor and mostly governed by electronic excitations. In this case, for desorbed molecules with the highest translational energy ($E_{kin} > 0.67$eV) we find an isotope effect favouring the vibrational excitation of the light isotope by 6% respect to the heavy one. Nevertheless, these desorbed molecules represent only around 1 % of the total desorption yield.

Our findings clearly point out that the CO photodesorption process from high covered CO/Pd(111) surface at high laser fluence, 130 J/m^2, is dominated by a phonon-mediated mechanism. Also, we have demonstrated with our computationally efficient methodology that even for a high fluence, the complete photodesorption process takes several tens of picoseconds to finalize. This complements previous experimental measurements made for the same system but lower laser fluences [9], between 50 and 80 J/m^2. Interestingly, in these studies a further phenomenological three temperature model analysis of two pulse correlation results suggested that CO femtosecond photodesorption is primarily driven by an electron-mediated energy transfer to adsorbates for CO coverages ranging from 0.24 ML to 0.75 ML, which contrasts with our molecular dynamics simulations at higher fluence. Therefore, this work motivates further systematic theoretical investigations on the role of laser-excited electrons and hot phonons in the desorption of CO at lower fluence regime and demonstrates the suitability of our methodology to simulate the complete photo-induced process in reasonable computational times.

Declaration of Competing Interest

The authors declare that they have no known competing financial interests or personal relationships that could have appeared to influence the work reported in this paper.

Acknowledgement

We thank Prof. Bin Jiang for providing us the EANN code and for his fruitful suggestions during the preparation of this work. The authors acknowledge financial support by the Gobierno Vasco-UPV/EHU Project No. IT1246-19, the Spanish Ministerio de Ciencia e Innovación [Grant No. PID2019-107396 GB-I00/AEI/10.13039/501100011033], and the Education Department of the Basque Government [IKUR strategic plan]. This work has been supported in part by Croatian Science Foundation under the project UIP-2020–02-5675. This research was conducted in the scope of the Transnational Common Laboratory (LTC) "QuantumChemPhys - Theoretical Chemistry and Physics at the Quantum Scale". Computational resources were provided by the DIPC computing center.

References

[1] C. Frischkorn, M. Wolf, Femtochemistry at metal surfaces: Nonadiabatic reaction dynamics, Chem. Rev. 106 (10) (2006) 4207–4233, https://doi.org/10.1021/cr050161r.
[2] H. Guo, P. Saalfrank, T. Seideman, Theory of photoinduced surface reactions of admolecules, Prog. Surf. Sci. 62 (7) (1999) 239–303, https://doi.org/10.1016/S0079-6816(99)00013-1.
[3] P. Saalfrank, Quantum dynamical approach to ultrafast molecular desorption from surfaces, Chem. Rev. 106 (10) (2006) 4116–4159, https://doi.org/10.1021/cr0501691.
[4] F. Budde, T.F. Heinz, M.M.T. Loy, J.A. Misewich, F. de Rougemont, H. Zacharias, Femtosecond time-resolved measurement of desorption, Phys. Rev. Lett. 66 (1991) 3024–3027, https://doi.org/10.1103/PhysRevLett.66.3024.
[5] J.A. Misewich, T.F. Heinz, D.M. Newns, Desorption induced by multiple electronic transitions, Phys. Rev. Lett. 68 (1992) 3737–3740, https://doi.org/10.1103/PhysRevLett.68.3737.
[6] M. Bonn, S. Funk, C. Hess, D.N. Denzler, C. Stampfl, M. Scheffler, M. Wolf, G. Ertl, Phonon- versus electron-mediated desorption and oxidation of CO on Ru(0001), Science 285 (5430) (1999) 1042–1045, https://doi.org/10.1126/science.285.5430.1042.
[7] D.N. Denzler, C. Frischkorn, C. Hess, M. Wolf, G. Ertl, Electronic excitation and dynamic promotion of a surface reaction, Phys. Rev. Lett. 91 (2003) 226102, https://doi.org/10.1103/PhysRevLett.91.226102.
[8] P. Szymanski, A.L. Harris, N. Camillone, Adsorption-state-dependent subpicosecond photoinduced desorption dynamics, J. Chem. Phys. 126 (21) (2007) 214709, https://doi.org/10.1063/1.2735594.
[9] S.-Y. Hong, P. Xu, N.R. Camillone, M.G. White, N. Camillone III, Adlayer structure dependent ultrafast desorption dynamics in carbon monoxide adsorbed on Pd (111), J. Chem. Phys. 145 (2016), 014704, https://doi.org/10.1063/1.4954408.
[10] S. Deliwala, R. Finlay, J. Goldman, T. Her, W. Mieher, E. Mazur, Surface femtochemistry of 0_2 and CO on Pt(111), Chem. Phys. Lett. 242 (6) (1995) 617–622, https://doi.org/10.1016/0009-2614(95)00791-2.
[11] S. Funk, M. Bonn, D.N. Denzler, C. Hess, M. Wolf, G. Ertl, Desorption of CO from Ru (001) induced by near-infrared femtosecond laser pulses, J. Chem. Phys. 112 (22) (2000) 9888–9897, https://doi.org/10.1063/1.481626.
[12] C. Hess, S. Funk, M. Bonn, D. Denzler, M. Wolf, G. Ertl, Femtosecond dynamics of chemical reactions at surfaces, Appl. Phys. A 71 (2000) 477–483, https://doi.org/10.1007/s003390000703.
[13] D.P. Quinn, T.F. Heinz, Observation of an isotope effect in femtosecond laser-induced desorption of O_2/Pd(111), J. Vac. Sci. Technol. A 21 (4) (2003) 1312–1316, https://doi.org/10.1116/1.1580486.
[14] S.I. Anisimov, B.L. Kapeliovich, T.L. Perel'man, Electron emission from metal surfaces exposed to ultrashort laser pulses, Sov. Phys. JETP 39 (1974) 375–377.
[15] C. Springer, M. Head-Gordon, J.C. Tully, Simulations of femtosecond laser-induced desorption of CO from Cu(100), Surf. Sci. 320 (1) (1994) L57–L62, https://doi.org/10.1016/0039-6028(94)00569-9.
[16] C. Springer, M. Head-Gordon, Simulations of the femtosecond laser-induced desorption of CO from Cu(100) at 0.5 ML coverage, Chem. Phys. 205 (1) (1996) 73–89, https://doi.org/10.1016/0301-0104(95)00316-9.
[17] T. Vazhappilly, T. Klamroth, P. Saalfrank, R. Hernandez, Femtosecond-laser desorption of H_2 (D_2) from Ru(0001): Quantum and classical approaches, J. Phys. Chem. C 113 (2009) 7790–7801, https://doi.org/10.1021/jp810709k.
[18] G. Füchsel, T. Klamroth, J.C. Tremblay, P. Saalfrank, Stochastic approach to laser-induced ultra fast dynamics: The desorption of H_2/D_2 from Ru(0001), Phys. Chem. Chem. Phys. 12 (2010) 14082–14094, https://doi.org/10.1039/C0CP00895H.
[19] G. Füchsel, T. Klamroth, S. Monturet, P. Saalfrank, Dissipative dynamics within the electronic friction approach: The femtosecond laser desorption of H_2/D_2 from Ru (0001), Phys. Chem. Chem. Phys. 13 (2011) 8659–8670, https://doi.org/10.1039/C0CP02086A.
[20] I. Lonari, M. Alducin, P. Saalfrank, J.I. Juaristi, Femtosecond-laser-driven molecular dynamics on surfaces: Photodesorption of molecular oxygen from Ag (110), Phys. Rev. B 93 (2016) 014301, https://doi.org/10.1103/PhysRevB.93.014301.
[21] I. Lončarić, M. Alducin, P. Saalfrank, J.I. Juaristi, Femtosecond laser pulse induced desorption: a molecular dynamics simulation, Nucl. Instrum. Methods B 382 (2016) 114–118, https://doi.org/10.1016/j.nimb.2016.02.051.
[22] R. Scholz, G. Floß, P. Saalfrank, G. Füchsel, I. Lonari, J.I. Juaristi, Femtosecond-laser induced dynamics of co on Ru(0001): Deep insights from a hot-electron friction model including surface motion, Phys. Rev. B 94 (2016) 165447, https://doi.org/10.1103/PhysRevB.94.165447.
[23] I. Lonari, G. Füchsel, J.I. Juaristi, P. Saalfrank, Strong anisotropic interaction controls unusual sticking and scattering of CO at Ru(0001), Phys. Rev. Lett. 119 (2017) 146101, https://doi.org/10.1103/PhysRevLett.119.146101.
[24] R. Scholz, S. Lindner, I. Lonari, J.C. Tremblay, J.I. Juaristi, M. Alducin, P. Saalfrank, Vibrational response and motion of carbon monoxide on Cu(100) driven by femtosecond laser pulses: Molecular dynamics with electronic friction, Phys. Rev. B 100 (2019) 245431, https://doi.org/10.1103/PhysRevB.100.245431.
[25] M. Alducin, R. Díez Muiño, J.I. Juaristi, Non-adiabatic effects in elementary reaction processes at metal surfaces, Prog. Surf. Sci. 92 (4) (2017) 317–340, https://doi.org/10.1016/j.progsurf.2017.09.002.
[26] M. Blanco-Rey, J.I. Juaristi, R. Díez Muiño, H.F. Busnengo, G.J. Kroes, M. Alducin, Electronic friction dominates hydrogen hot-atom relaxation on Pd(100), Phys. Rev. Lett. 112 (2014) 103203, https://doi.org/10.1103/PhysRevLett.112.103203.
[27] D. Novko, M. Blanco-Rey, J.I. Juaristi, M. Alducin, Ab Initio molecular dynamics with simultaneous electron and phonon excitations: Application to the relaxation of hot atoms and molecules on metal surfaces, Phys. Rev. B 92 (2015) 201411, https://doi.org/10.1103/PhysRevB.92.201411.
[28] D. Novko, M. Blanco-Rey, J.I. Juaristi, M. Alducin, Energy loss in gas-surface dynamics: Electron-hole pair and phonon excitation upon adsorbate relaxation, Nucl. Instrum. Methods B 382 (2016) 26–31, https://doi.org/10.1016/j.nimb.2016.02.031.
[29] D. Novko, M. Blanco-Rey, M. Alducin, J.I. Juaristi, Surface electron density models for accurate ab initio molecular dynamics with electronic friction, Phys. Rev. B 93 (2016) 245435, https://doi.org/10.1103/PhysRevB.93.245435.
[30] D. Novko, I. Lonari, M. Blanco-Rey, J.I. Juaristi, M. Alducin, Energy loss and surface temperature effects in ab initio molecular dynamics simulations: N adsorption on Ag(111) as a case study, Phys. Rev. B 96 (2017) 085437, https://doi.org/10.1103/PhysRevB.96.085437.
[31] X. Zhou, L. Zhang, B. Jiang, Hot-atom-mediated dynamical displacement of co adsorbed on cu(111) by incident h atoms: An ab initio molecular dynamics study, J. Phys. Chem. C 122 (27) (2018) 15485–15493, https://doi.org/10.1021/acs.jpcc.8b04123.
[32] X. Zhou, Y. Zhang, H. Guo, B. Jiang, Towards bridging the structure gap in heterogeneous catalysis: the impact of defects in dissociative chemisorption of methane on ir surfaces, Phys. Chem. Chem. Phys. 23 (2021) 4376–4385, https://doi.org/10.1039/D0CP06535H.
[33] G.-J. Kroes, J.I. Juaristi, M. Alducin, Vibrational excitation of h2 scattering from cu (111): Effects of surface temperature and of allowing energy exchange with the surface, J. Phys. Chem. C 121 (25) (2017) 13617–13633, https://doi.org/10.1021/acs.jpcc.7b01096.
[34] G. Füchsel, X. Zhou, B. Jiang, J.I. Juaristi, M. Alducin, H. Guo, G.-J. Kroes, Reactive and nonreactive scattering of HCl from Au(111): An ab initio molecular dynamics study, J. Phys. Chem. C 123 (4) (2019) 2287–2299, https://doi.org/10.1021/acs.jpcc.8b10686.
[35] L. Zhou, B. Jiang, M. Alducin, H. Guo, Communication: Fingerprints of reaction mechanisms in product distributions: Eley-rideal-type reactions between D and CD_3/Cu(111), J. Chem. Phys. 149 (3) (2018), 031101, https://doi.org/10.1063/1.5039749.

[36] L. Zhou, X. Zhou, M. Alducin, L. Zhang, B. Jiang, H. Guo, Ab initio molecular dynamics study of the Eley-Rideal reaction of HCl-Au(111) -> HCl + Au(111): Impact of energy dissipation to surface phonons and electron-hole pairs, J. Chem. Phys. 148 (1) (2018), 014702, https://doi.org/10.1063/1.5016054.

[37] J. Chen, X. Zhou, B. Jiang, Eley Rideal recombination of hydrogen atoms on Cu (111): Quantitative role of electronic excitation in cross sections and product distributions, J. Chem. Phys. 150 (6) (2019), 061101, https://doi.org/10.1063/1.5086326.

[38] P. Saalfrank, J.I. Juaristi, M. Alducin, M. Blanco-Rey, R. Díez Muiño, Vibrational lifetimes of hydrogen on lead films: An ab initio molecular dynamics with electronic friction (AIMDEF) study, J. Chem. Phys. 141 (23) (2014), 234702, https://doi.org/10.1063/1.4903309.

[39] J.I. Juaristi, M. Alducin, P. Saalfrank, Femtosecond laser induced desorption of H_2, D_2, and hd from Ru(0001): Dynamical promotion and suppression studied with ab initio molecular dynamics with electronic friction, Phys. Rev. B 95 (2017), 125439, https://doi.org/10.1103/PhysRevB.95.125439.

[40] M. Alducin, N. Camillone, S.-Y. Hong, J.I. Juaristi, Electrons and phonons cooperate in the laser-induced desorption of CO from Pd(111), Phys. Rev. Lett. 123 (2019), 246802, https://doi.org/10.1103/PhysRevLett.123.246802.

[41] O.T. Unke, S. Chmiela, H.E. Sauceda, M. Gastegger, I. Poltavsky, K.T. Schütt, A. Tkatchenko, K.-R. Müller, Machine learning force fields, Chem. Rev. 121 (16) (2021) 10142–10186, https://doi.org/10.1021/acs.chemrev.0c01111.

[42] J. Behler, Constructing high-dimensional neural network potentials: A tutorial review, Int. J. Quantum. Chem. 115 (2015) 1032–1050, https://doi.org/10.1002/qua.24890.

[43] V. Quaranta, M. Hellström, J. Behler, Proton-transfer mechanisms at the water-zno interface: The role of presolvation, J. Phys. Chem. Lett. 8 (7) (2017) 1476–1483, https://doi.org/10.1021/acs.jpclett.7b00358.

[44] M. Hellström, V. Quaranta, J. Behler, One-dimensional vs. two-dimensional proton transport processes at solid-liquid zinc-oxide-water interfaces, Chem. Sci. 10 (2019) 1232–1243, https://doi.org/10.1039/C8SC03033B.

[45] H. Ghorbanfekr, J. Behler, F.M. Peeters, Insights into water permeation through hbn nanocapillaries by ab initio machine learning molecular dynamics simulations, J. Phys. Chem. Lett. 11 (17) (2020) 7363–7370, https://doi.org/10.1021/acs.jpclett.0c01739.

[46] B. Jiang, H. Guo, Dynamics of water dissociative chemisorption on Ni(111): Effects of impact sites and incident angles, Phys. Rev. Lett. 114 (2015), 166101, https://doi.org/10.1103/PhysRevLett.114.166101.

[47] X. Shen, J. Chen, Z. Zhang, K. Shao, D.H. Zhang, Methane dissociation on Ni(111): A fifteen-dimensional potential energy surface using neural network method, J. Chem. Phys 143 (14) (2015), 144701, https://doi.org/10.1063/1.4932226.

[48] B. Kolb, X. Luo, X. Zhou, B. Jiang, H. Guo, High-dimensional atomistic neural network potentials for molecule-surface interactions: HCl scattering from Au(111), J. Phys. Chem. Lett. 8 (3) (2017) 666–672, https://doi.org/10.1021/acs.jpclett.6b02994.

[49] K. Shakouri, J. Behler, J. Meyer, G.-J. Kroes, Accurate neural network description of surface phonons in reactive gas-surface dynamics: N_2 + Ru(0001), J. Phys. Chem. Lett. 8 (10) (2017) 2131–2136, https://doi.org/10.1021/acs.jpclett.7b00784.

[50] Q. Liu, X. Zhou, L. Zhou, Y. Zhang, X. Luo, H. Guo, B. Jiang, Constructing high-dimensional neural network potential energy surfaces for gas-surface scattering and reactions, J. Phys. Chem. C 122 (3) (2018) 1761–1769, https://doi.org/10.1021/acs.jpcc.7b12064.

[51] J. Chen, X. Zhou, Y. Zhang, B. Jiang, Vibrational control of selective bond cleavage in dissociative chemisorption of methanol on Cu(111), Nat. Commun. 9 (1) (2018), 4039, https://doi.org/10.1038/s41467-018-06478-6.

[52] K. Shakouri, J. Behler, J. Meyer, G.-J. Kroes, Analysis of energy dissipation channels in a benchmark system of activated dissociation: N_2 on Ru(0001), J. Phys. Chem. C 122 (41) (2018) 23470–23480, https://doi.org/10.1021/acs.jpcc.8b06729.

[53] N. Gerrits, K. Shakouri, J. Behler, G.-J. Kroes, Accurate probabilities for highly activated reaction of polyatomic molecules on surfaces using a high-dimensional neural network potential: CHD_3 + Cu(111), J. Phys. Chem. Lett. 10 (8) (2019) 1763–1768, https://doi.org/10.1021/acs.jpclett.9b00560.

[54] Y. Zhang, X. Zhou, B. Jiang, Bridging the gap between direct dynamics and globally accurate reactive potential energy surfaces using neural networks, J. Phys. Chem. Lett. 10 (6) (2019) 1185–1191, https://doi.org/10.1021/acs.jpclett.9b00085.

[55] M. Huang, X. Zhou, Y. Zhang, L. Zhou, M. Alducin, B. Jiang, H. Guo, Adiabatic and nonadiabatic energy dissipation during scattering of vibrationally excited CO from Au(111), Phys. Rev. B 100 (2019), 201407, https://doi.org/10.1103/PhysRevB.100.201407.

[56] B. Jiang, J. Li, H. Guo, High-fidelity potential energy surfaces for gas-phase and gas-surface scattering processes from machine learning, J. Phys. Chem. Lett. 11 (13) (2020) 5120–5131, https://doi.org/10.1021/acs.jpclett.0c00989.

[57] N. Gerrits, J. Geweke, E.W.F. Smeets, J. Voss, A.M. Wodtke, G.-J. Kroes, Closing the gap between experiment and theory: Reactive scattering of HCl from Au(111), J. Phys. Chem. C 124 (29) (2020) 15944–15960, https://doi.org/10.1021/acs.jpcc.0c03756.

[58] A. Rivero Santamaría, M. Ramos, M. Alducin, H.F. Busnengo, R. Díez Muiño, J. I. Juaristi, High-dimensional atomistic neural network potential to study the alignment-resolved O_2 scattering from highly oriented pyrolytic graphite, J. Phys. Chem. A 125 (12) (2021) 2588–2600, https://doi.org/10.1021/acs.jpca.1c00835.

[59] J. Behler, M. Parrinello, Generalized neural-network representation of high-dimensional potential-energy surfaces, Phys. Rev. Lett. 98 (14) (2007) 1–4, https://doi.org/10.1103/PhysRevLett.98.146401.

[60] J. Behler, Four generations of high-dimensional neural network potentials, Chem. Rev. 121 (16) (2021) 10037–10072, https://doi.org/10.1021/acs.chemrev.0c00868.

[61] Y. Zhang, C. Hu, B. Jiang, Embedded atom neural network potentials: Efficient and accurate machine learning with a physically inspired representation, J. Phys. Chem. Lett. 10 (17) (2019) 4962–4967, https://doi.org/10.1021/acs.jpclett.9b02037.

[62] L. Zhu, Y. Zhang, L. Zhang, X. Zhou, B. Jiang, Unified and transferable description of dynamics of H_2 dissociative adsorption on multiple copper surfaces via machine learning, Phys. Chem. Chem. Phys. 22 (2020) 13958–13964, https://doi.org/10.1039/D0CP02291H.

[63] A. Serrano-Jiménez, A.P.S. Muzas, Y. Zhang, J. Ovčar, B. Jiang, I. Lončarić, J. I. Juaristi, M. Alducin, Photoinduced Desorption Dynamics of CO from Pd(111): A Neural Network Approach, J. Chem. Theory Comput. 17 (8) (2021) 4648–4659, https://doi.org/10.1021/acs.jctc.1c00347.

[64] P. Szymanski, A. Harris, N. Camillone, Temperature-dependent electron-mediated coupling in subpicosecond photoinduced desorption, Surf. Sci. 601 (16) (2007) 3335–3349, https://doi.org/10.1016/j.susc.2007.06.004.

[65] S. Nosé, A unified formulation of the constant temperature molecular dynamics methods, J. Chem. Phys. 81 (1) (1984) 511–519, https://doi.org/10.1063/1.447334.

[66] W.G. Hoover, Canonical dynamics: Equilibrium phase-space distributions, Phys. Rev. A 31 (1985) 1695–1697, https://doi.org/10.1103/PhysRevA.31.1695.

[67] J.I. Juaristi, M. Alducin, R. Díez Muiño, H.F. Busnengo, A. Salin, Role of electron-hole pair excitations in the dissociative adsorption of diatomic molecules on metal surfaces, Phys. Rev. Lett. 100 (11) (2008), 116102, https://doi.org/10.1103/PhysRevLett.100.116102.

[68] J. Ischtwan, M.A. Collins, Molecular potential energy surfaces by interpolation, J. Chem. Phys. 100 (11) (1994) 8080–8088, https://doi.org/10.1063/1.466801.

[69] R.P. Bettens, M.A. Collins, Learning to interpolate molecular potential energy surfaces with confidence: a Bayesian approach, J. Chem. Phys. 111 (3) (1999) 816–826, https://doi.org/10.1063/1.479368.

[70] Q. Lin, L. Zhang, Y. Zhang, B. Jiang, Searching configurations in uncertainty space: Active learning of high-dimensional neural network reactive potentials, J. Chem. Theory Comput. 17 (5) (2021) 2691–2701, https://doi.org/10.1021/acs.jctc.1c00166.

[71] L. Raff, M. Malshe, M. Hagan, D. Doughan, M. Rockley, R. Komanduri, Ab initio potential-energy surfaces for complex, multichannel systems using modified novelty sampling and feedforward neural networks, J. Chem. Phys. 122 (8) (2004), 084104, https://doi.org/10.1063/1.1850458.

[72] J. Ludwig, D.G. Vlachos, Ab initio molecular dynamics of hydrogen dissociation on metal surfaces using neural networks and novelty sampling, J. Chem. Phys. 127 (15) (2007), 154716, https://doi.org/10.1063/1.2794338.

[73] G.J. Kroes, E. Pijper, A. Salin, Dissociative chemisorption of H_2 on the Cu(110) surface: A quantum and quasiclassical dynamical study, J. Chem. Phys. 127 (16) (2007), 164722, https://doi.org/10.1063/1.2798112.

[74] E.B. Wilson, Probable inference, the law of succession, and statistical inference, J. Am. Stat. Assoc. 22 (158) (1927) 209–212, https://doi.org/10.2307/2276774.